Deep learning predicted elliptic flow of identified particles in heavy-ion collisions at the RHIC and LHC energies

Neelkamal Mallick[1,*] Suraj Prasad[1,†] Aditya Nath Mishra[2,4,‡]
Raghunath Sahoo[1,§] and Gergely Gábor Barnaföldi[3,‖]

[1]*Department of Physics, Indian Institute of Technology Indore, Simrol, Indore 453552, India*
[2]*Department of Physics, School of Applied Sciences, REVA University, Bangalore 560064, India*
[3]*Wigner Research Center for Physics, 29-33 Konkoly-Thege Miklós Str., H-1121 Budapest, Hungary*
[4]*Department of Physics, University Centre For Research & Development (UCRD),*
Chandigarh University, Mohali, Punjab 140413, India

Recent developments of a deep learning feed-forward network for estimating elliptic flow (v_2) coefficients in heavy-ion collisions have shown the prediction power of this technique. The success of the model is mainly the estimation of v_2 from final-state particle kinematic information and learning the centrality and transverse momentum (p_T) dependence of v_2. The deep learning model is trained with Pb-Pb collisions at $\sqrt{s_{NN}} = 5.02$ TeV minimum bias events simulated with a multiphase transport model. We extend this work to estimate v_2 for light-flavor identified particles such as $\pi^{\pm}$, $K^{\pm}$, and $p + \bar{p}$ in heavy-ion collisions at RHIC and LHC energies. The number-of-constituent-quark scaling is also shown. The evolution of the p_T-crossing point of $v_2(p_T)$, depicting a change in baryon-meson elliptic flow at intermediate p_T, is studied for various collision systems and energies. The model is further evaluated by training it for different p_T regions. These results are compared with the available experimental data wherever possible.

I. INTRODUCTION

Relativistic heavy-ion collisions have been studied extensively for decades in experiments at the Large Hadron Collider (LHC) and Relativistic Heavy Ion collider (RHIC). The formation of a deconfined thermalized medium of quarks and gluons has already been established in such collisions [1]. This hot and dense medium of strongly interacting matter is known as the quark-gluon plasma (QGP). Direct probes for studying the properties of QGP are not available owing to the behavior of the strongly interacting matter. However, the signatures of the formation of QGP could be studied using various indirect effects such as jet quenching, strangeness enhancement, and quarkonia

*Neelkamal.Mallick@cern.ch
†Suraj.Prasad@cern.ch
‡Aditya.Nath.Mishra@cern.ch
§Corresponding author.
Raghunath.Sahoo@cern.ch
‖Barnafoldi.Gergely@wigner.hu

suppression, just to name a few. Another crucial observable, which is widely studied to investigate the properties of QGP in heavy-ion collisions, is the transverse collective flow [2]. This transverse collective flow is anisotropic and depends on the equation of state and transport coefficients of the system. Due to the almond-shaped, elliptical nuclear overlap region in noncentral heavy-ion collisions, the initial state has finite spatial anisotropy, further developing the final-state momentum anisotropy of the emitted particles. This momentum anisotropy could be expressed as the coefficients of the Fourier expansion of the azimuthal momentum distribution of the produced particles. Finite azimuthal anisotropy has been well observed in heavy-ion collision experiments so far [3–6]. The second-order flow coefficient, also known as the elliptic flow (v_2), which is believed to be driven mainly by the geometry of the distributed nucleons in the nuclear overlap region during a noncentral heavy-ion collision, provides the dominant contribution to the overall azimuthal anisotropy.

Different hydrodynamic model calculations suggest that elliptic flow builds up in the early partonic phases of the QGP and evolves through hadronic rescatterings in the hadronic phase. Theoretically, azimuthal anisotropy is thus understood to have consequences from (ideal) fluid dynamics applied to the QGP phase and kinetic descriptions applied to the microscopic hadron cascade phase [7–11].

Therefore, to understand the interplay of partonic and hadronic phases in the evolution of collective flow, it becomes necessary to study the elliptic flow for different identified particles. The competing effects of radial (symmetric) flow and hadronic rescatterings could also be studied by estimating the elliptic flow of identified particles.

Another exciting thing that has been observed in heavy-ion collisions is that the v_2 of baryons is larger than that of mesons in the intermediate-p_T range $(2.0 \lesssim p_T \lesssim 5.0 \, \text{GeV}/c)$. This is usually attributed to particle production by constituent quark coalescence [12]. According to this theory, the development of hydrodynamic flow happens in the early deconfined partonic phase and is subsequently transferred to the hadrons by hadronization through the quark coalescence mechanism [13–15]. In an ideal case, this behavior should lead to the number-of-constituent-quark (NCQ) scaling of the observed flow for baryons and mesons and, thus, strongly hints at the appearance of collectivity at the early deconfined partonic level. In Au-Au collisions at $\sqrt{s_{NN}} = 200$ GeV, the scaling holds only approximately [16]. However, in Pb-Pb collisions at $\sqrt{s_{NN}} = 2.76$ and 5.02 TeV, the scaling holds only up to a level of $\pm 20\%$ [4,17,18].

There are several methods to estimate the flow coefficients, such as the complex reaction plane identification method [19], the cumulant method [20], the Lee-Yang zeros method [21], and the principal component analysis method [22–25]. For the first time, it has been shown that deep learning models, based on a machine learning (ML) framework, could also be used to estimate the flow coefficients; in particular, the results of elliptic flow calculations have been emphasized [26].

The motivation of the present study is to prepare a deep learning framework for the estimation of elliptic flow from final-state particle kinematic information. This is an attempt to see whether an ML model can learn from final-state particle correlations to predict any physical observable of interest. Since the elliptic flow is influenced by several factors—such as the collision centrality, energy, system size, particle mass, particle species, and transverse momentum—it will be interesting to see how well the deep learning model is able to preserve these dependencies. The trained model is found to be faster and more efficient in computing the flow coefficient than some of the traditional methods such as the multiparticle cumulant method.

The proposed deep learning model successfully learns and preserves the centrality and transverse momentum (p_T) dependence of v_2. It is also shown to perform steadily and accurately when confronted with a data set with additional noise. In this work, we estimate the elliptic flow coefficient for identified stable light hadrons like $\pi^\pm$, $K^\pm$, and $p + \bar{p}$ in Au-Au collisions at $\sqrt{s_{NN}} = 200$ GeV, Pb-Pb collisions at $\sqrt{s_{NN}} = 2.76$ and 5.02 TeV, and Xe-Xe collisions at $\sqrt{s_{NN}} = 5.44$ TeV for (0–10)%, (40–50)%, and (60–70)% centrality classes by using the deep learning estimator mentioned in Ref. [26]. The NCQ scaling is also

studied for these collision systems. The evolution of the p_T-crossing point of $v_2(p_T)$, depicting a change in baryon-meson elliptic flow at intermediate p_T, is studied for the above-mentioned collision systems at different energies. The prediction capability of the model is further evaluated by training it with particles in different p_T regions.

The paper is organized as follows. We briefly introduce the event generation using a multiphase transport model (AMPT) and the target observable—the elliptic flow—in Sec. II. The proposed deep learning estimator is described in Sec. III along with some performance plots of the model. In Sec. IV we describe the results, and we conclude with a summary in Sec. V.

II. EVENT GENERATION AND TARGET OBSERVABLE

In order to train the deep learning-based ML algorithm to estimate the elliptic flow, we use an AMPT model to simulate the data set, a short description of which is provided in this section, along with the elliptic flow.

A. AMPT model

AMPT is a Monte Carlo–based event simulator that is used to generate ultrarelativistic p-A and A-A collisions at RHIC and LHC energies [27]. AMPT has four components: (1) the initialization of collisions using the heavy-ion jet interaction generator model (HIJING) [28], (2) parton transport using Zhang's parton cascade model [29], (3) the hadronization of the partons using the spatial coalescence mechanism in the string-melting version of AMPT and the Lund string fragmentation model in the default version of AMPT [30,31], and (4) hadron transport using a relativistic transport model (ART) [32,33]. The AMPT model is extensively used to study the properties of hot and dense media formed in relativistic heavy-ion collisions, including the elliptic flow coefficient. The string-melting mode of AMPT describes the elliptic flow well in the intermediate transverse momentum region using the quark coalescence mechanism for hadronization [34–36]. Hence, in this study we incorporate the string-melting mode with AMPT version 2.26t9b. The AMPT settings used in this work are the same as those reported in Refs. [37–40]. We use the impact parameter slicing definition of the centrality, and the corresponding impact parameter values are taken from Ref. [41].

B. Elliptic flow

Anisotropic flow is one of the key observables in the evolution of QGP in noncentral relativistic heavy-ion collisions. The pressure gradient formed in the hot and dense medium due to the initial-state spatial anisotropy can transform into final-state momentum azimuthal anisotropy. The azimuthal anisotropy depends on the equation of state as well as the transport coefficients of the medium formed.

It can be quantified by the coefficients of the Fourier expansion of the azimuthal momentum distribution of particles, given by [42]

$$\frac{dN}{d\phi} = \frac{1}{2\pi}\left(1 + 2\sum_{n=1}^{\infty} v_n \cos[n(\phi - \psi_n)]\right). \qquad (1)$$

Here, $v_n = \langle\cos[n(\phi - \psi_n)]\rangle$ denotes the nth-order anisotropic flow coefficient, ϕ is the azimuthal angle, and ψ_n is the nth harmonic symmetry plane angle. The second-order anisotropic flow coefficient (v_2) is called the elliptic flow and has a major contribution from the initial eccentricity. In order to calculate the elliptic flow event by event, we use the event plane method [43]. Here, we set $\psi_R = 0$, which makes $v_2 = \langle\cos(2\phi)\rangle$. The average is taken over all charged particles in an event.

III. DEEP LEARNING ESTIMATOR

ML is a branch of artificial intelligence that learns correlations from the data to map the input and output observables. Boosted decision trees, deep neural networks, convolutional neural networks, etc., can learn suitable correlations from the data through model training and help us map complex nonlinear observables whose mapping functions cannot be trivially written in a sequential algorithm. Heavy-ion collisions at LHC energies produce thousands of final-state hadrons, each carrying specific kinematic information and evolving through different physical processes, which makes the system complex and nonlinear and probing the underlying dynamics challenging. ML has been used by the collider physics community for more than a decade to extract the desired physics information from such complex systems [44–50]. In this study, we apply a deep neural network (DNN)-based ML algorithm to determine the elliptic flow coefficient, which takes p_T, mass, and $\log\sqrt{(s_{NN}/s_0)}$-weighted $(\eta - \phi)$ binned values as different features of the input to the model, as described in detail in Ref. [26]. The charged particle tracks in $|\eta| < 0.8$, with $p_T \geq 0.15$ GeV/c and $\phi \in [0, 2\pi]$, are considered for the training. Also, this is an inverse supervised regression problem, and thus the output labels of the DNN model—the elliptic flow coefficients—are estimated using the event plane method from the AMPT simulation on an event-by-event basis. The model is trained with minimum bias Pb-Pb collisions at $\sqrt{s_{NN}} = 5.02$ TeV. The input data set is divided by the number of events in 8:1:1 for making the training, validation, and testing data set, respectively.

The DNN architecture used in this paper for the regression problem consists of one input layer, four dense hidden layers, and one output layer, as shown in Fig. 1. The input layer with 3072 features is mapped to the output layer via four hidden layers, one after another, each having 128, 256, 256, and 256 nodes, respectively. All four hidden
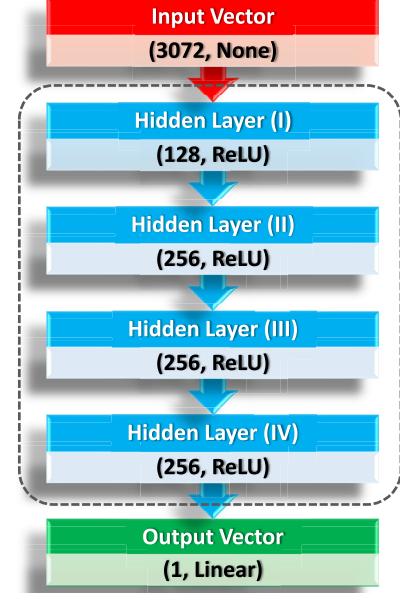

FIG. 1. Schematics of the deep neural network architecture used in this work containing one input layer, followed by four hidden dense layers, and one output layer. The number of nodes and the type of activation function used in each layer is mentioned.

dense layers use the rectified linear unit as the activation function [51], and the output layer has a single node with a linear activation function. The DNN model uses the *adam* algorithm as the optimizer [52] with the mean-squared error as the loss function, the details of which can be found in Ref. [26]. We have not implemented any L2 regularization or dropout as these seem to hamper the performance of the DNN, as shown in Fig. 2. The mean absolute error (MAE) of elliptic flow (Δv_2), defined in Eq. (2), decreases for an increase in λ and a decrease in P; however, Δv_2 is found to be the smallest for the case with no L2 regularization and
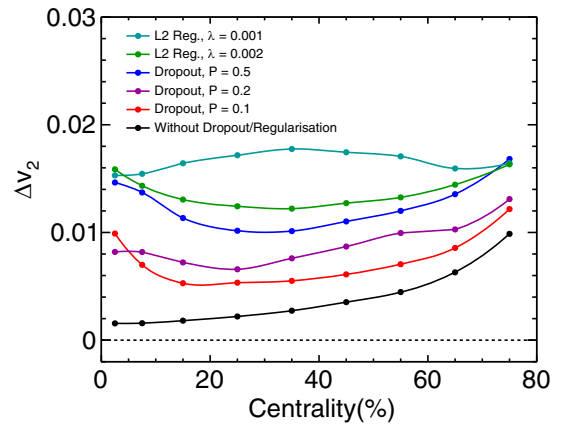

FIG. 2. Evolution of the MAE (Δv_2) as a function of centrality in Pb-Pb collisions at $\sqrt{s_{NN}} = 5.02$ TeV, with the model trained with L2 regularization and dropout with their respective hyperparameters.
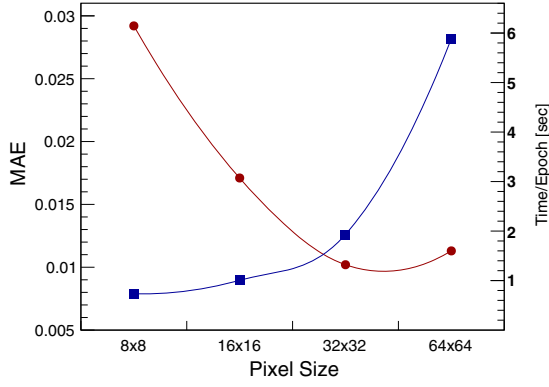
FIG. 3.   MAE for v_2 (dots) and time taken per epoch (squares) during the training of the DNN as a function of input pixel size.

dropout. λ and P are the hyperparameters in L2 regularization and dropout, respectively:

$$\Delta v_2 = \frac{1}{N_{\text{events}}} \sum_{n=1}^{N_{\text{events}}} |v_{2_n}^{\text{true}} - v_{2_n}^{\text{pred}}|. \qquad (2)$$

Figure 3 shows the choice of different bin sizes in $(\eta - \phi)$ space for the input with the corresponding MAE and the estimation for the training time as time/epoch in seconds. One can infer from the figure that as the bin size increases, the MAE decreases and the corresponding training time increases. However, the bin size 32×32 gives the optimum MAE and training time, which is used as the input binning for p_T, mass, and $\log \sqrt{(s_{\text{NN}}/s_0)}$ weighted in $(\eta - \phi)$ space. Thus, this results in a total of 3072 $(= 32 \times 32 \times 3)$ features per event as the input features. It is to be noted that the training time may differ from Fig. 3, depending on the type of CPU used. The time per epoch shown in Fig. 3 employs an Intel(R) Core(TM) i5-8279U CPU (released Q2 of 2019) with four cores (eight threads) clocked at a base frequency of 2.40 GHz and a max turbo boost frequency of 4.10 GHz [53]. The system has 8 GB of LPDDR3 RAM clocked at 2133 MHz. The data set with 3072 features per event is normalized with the L2 norm before the DNN is ready to take it as input.

Further quality assurance checks on the DNN model can be found in Ref. [26], which suggested that the model can successfully be used not only for different centralities but also in different energy data and gives reasonable results for a p_T-dependent v_2 while having trained with minimum bias events in Pb–Pb collisions at $\sqrt{s_{\text{NN}}} = 5.02$ TeV, event by event.

In this study, for the implementation of the DNN model, we use the KERAS v2.7.0 deep learning Application Programming Interface (API) [54] with TensorFlow v2.7.0 [55] in PYTHON along with the scikit-learn ML framework [56].

IV. RESULTS AND DISCUSSIONS

In this section, we begin with a comparison of the elliptic flow coefficients of $\pi^\pm$, $K^\pm$, and $p + \bar{p}$ predicted from the DNN estimator with the true values from AMPT simulation and ALICE results. We proceed to show the centrality, energy, and transverse momentum dependence of v_2, and also study whether the scaling properties of v_2 are encoded in the neural network. The evolution of the crossing point in p_T for baryon-meson v_2 separation in intermediate p_T and the effect of transverse-momentum-dependent training are also described in this section.

A. Comparing DNN predictions to AMPT and experimental data

Figure 4 shows the elliptic flow, $v_2(p_T)$, for identified $\pi^\pm$, $K^\pm$, and $p + \bar{p}$ in (40–50)% central Pb-Pb collisions at $\sqrt{s_{\text{NN}}} = 5.02$ TeV. To compare the AMPT and DNN outcomes with ALICE results [18], tracks with $p_T > 0.5$ GeV/c for midrapidity $|y| < 0.5$ are considered for this case. The magnitude of $v_2(p_T)$ increases with increasing p_T for all three particle species until it attains a maximum value around $p_T \approx 2.0$ GeV/c, and then it starts to decrease beyond this point. The values of $v_2(p_T)$ from AMPT obtained in this region (i.e., $p_T \lesssim 2.0$–3.0 GeV/c) is comparable in magnitude with ALICE results for the individual particle cases. However, beyond this transverse momentum value, AMPT fails to describe the data as $v_2(p_T)$ falls faster with increasing p_T since fragmentation becomes the preferred mode of hadronization at high-p_T.
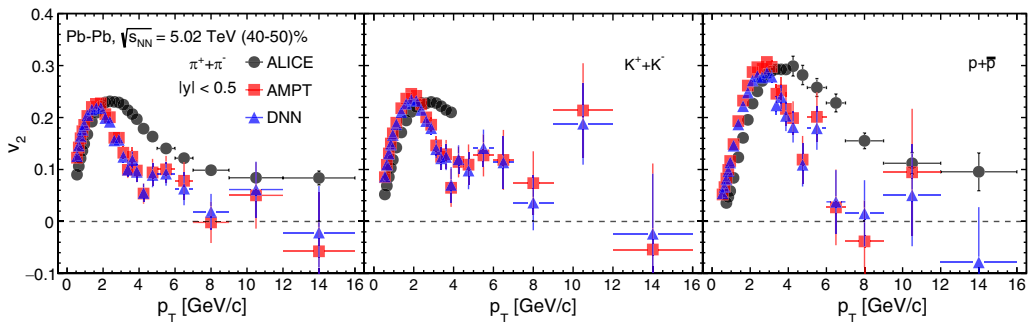

FIG. 4.   Elliptic flow (v_2) as a function of transverse momentum (p_T) for $\pi^\pm$, $K^\pm$, and $p + \bar{p}$ in (40–50)% central Pb-Pb collisions at $\sqrt{s_{\text{NN}}} = 5.02$ TeV. ALICE [18], AMPT, and DNN results are shown as dots, squares, and triangles, respectively.

It is interesting to note that DNN predictions agree with AMPT values quite nicely up to $p_T \lesssim 4.0$–6.0 GeV/c. Beyond this p_T, the values from DNN start to differ from the AMPT values. The DNN model is trained with Pb-Pb collisions in $\sqrt{s_{NN}} = 5.02$ TeV minimum bias events with the selection of all charged particles having $p_T > 0.15$ GeV/c in pseudorapidity, $|\eta| < 0.8$ simulated with AMPT. It is seen that the statistics in each p_T bin for all three particle types decreases to about a few hundred counts for $p_T \gtrsim 6.0$ GeV/c, which presents a few instances to the DNN model during the training process. For this reason, the mismatch between DNN and AMPT comes into the picture for $p_T \gtrsim 6.0$ GeV/c. For the above-mentioned reasons, this analysis is kept in the range $p_T < 3.0$ GeV/c for the rest of the plots where the Monte Carlo results and data are comparable.

B. Centrality and energy dependence of elliptic flow

Figure 5 represents the centrality dependence of $v_2(p_T)$ for $\pi^{\pm}$, $K^{\pm}$, and $p + \bar{p}$, and all charged hadrons ($h^{\pm}$) in Au-Au collisions at $\sqrt{s_{NN}} = 200$ GeV, Pb-Pb collisions at $\sqrt{s_{NN}} = 2.76$ and 5.02 TeV, and Xe-Xe collisions at $\sqrt{s_{NN}} = 5.44$ TeV for $(0$–$10)\%$, $(40$–$50)\%$, and $(60$–$70)\%$ centrality classes. The true values from AMPT and the predicted values from the DNN estimator are presented. As one moves from central to peripheral collisions, the magnitude of $v_2(p_T)$ keeps increasing for all particle types up to mid-central collisions, i.e., $(40$–$50)\%$, and then it starts to decrease. This is well understood from the fact that the initial geometrical anisotropy in the nuclear overlap region keeps increasing for peripheral collisions. However,
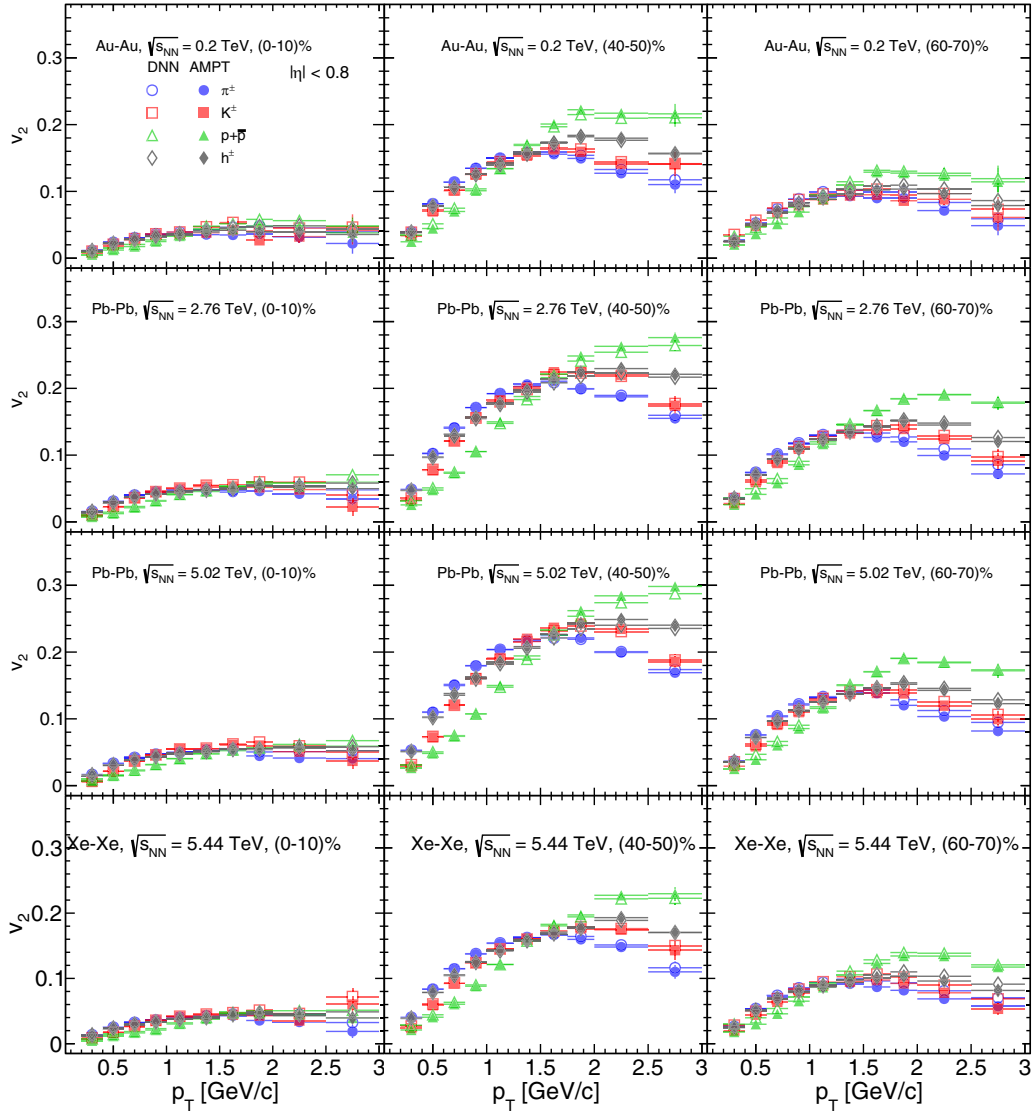

FIG. 5. Centrality dependence of $v_2(p_T)$ for $\pi^{\pm}$, $K^{\pm}$, and $p + \bar{p}$, and all charged hadrons ($h^{\pm}$). The values from AMPT and the predictions from DNN are shown.

for more peripheral collisions, i.e., (60–70)%, $v_2(p_T)$ gets reduced as the smaller size and shorter lifetime of the system do not allow the generation of large v_2. For $p_T \lesssim 1.5$ GeV/c, there is a mass ordering of $v_2(p_T)$ for different particles, meaning lighter particles have more v_2 than the heavier ones, where

$$v_2^{\pi^\pm} > v_2^{K^\pm} > v_2^{p+\bar{p}}. \tag{3}$$

This is understood as an effect of strong radial flow, which imposes an azimuthally symmetric velocity boost to all particles along with the anisotropic flow in the medium. In the intermediate p_T range, the baryon-meson v_2 gets separated as

$$v_2^{(\text{Baryons})} > v_2^{(\text{Mesons})}. \tag{4}$$

The baryon-meson v_2 separation could arise from the constituent quark coalescence mechanism embedded in the AMPT string-melting mode [57]. The DNN estimator, trained at the LHC energy, in Pb-Pb collisions for the $\sqrt{s_{NN}} = 5.02$ TeV minimum bias data set, can predict the identified particle v_2 for different collision systems at different collision energies. The mass ordering at low p_T and the grouping of particles based on their constituent quarks in the intermediate p_T range are learned and preserved by the DNN estimator.

Figure 6 shows the ratio of $v_2(p_T)$ estimated with the DNN model over the AMPT values for $\pi^\pm$, $K^\pm$, and $p + \bar{p}$, and all charged hadrons ($h^\pm$). For the (40–50)% centrality class, the DNN predictions for all particle types are in better agreement with the AMPT values as compared to the (0–10)% and (60–70)% centrality classes. In Ref. [26], while dealing with the centrality dependence of v_2 for all
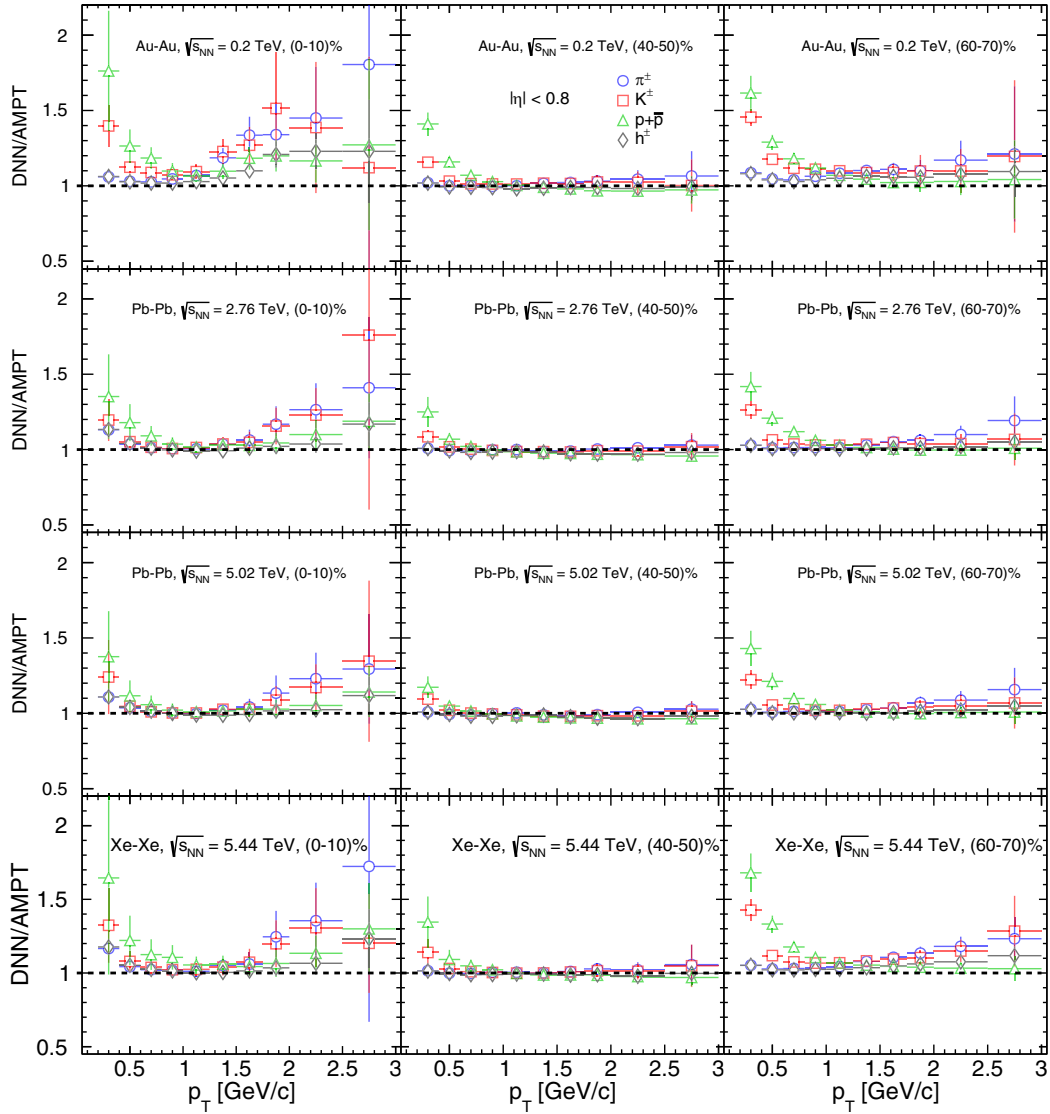

FIG. 6. DNN-to-AMPT ratio of $v_2(p_T)$ for $\pi^\pm$, $K^\pm$, and $p + \bar{p}$, and all charged hadrons ($h^\pm$).

charged hadrons, one can observe that the predictions for the most central and peripheral cases have larger statistical uncertainty than the mid-central cases. Here, Fig. 6 also suggests similar behavior. We argue that this is entirely statistics driven as the number of events in the extreme centrality bins is less in a minimum bias data set; hence, with the minimum bias training, the DNN model does not get enough examples to learn from these extreme domains. A similar argument could also be given for the slight mismatch of the proton v_2 at low p_T and the pion v_2 at intermediate p_T, where the respective statistics is comparably less. The solution to this problem could come from various collaborative learning models [58]. The same DNN model could be trained separately with centrality-wise data sets, unlike the minimum bias training to obtain a common set of model parameters. This could possibly take out the training sample bias due to the different number of events in different centrality bins, leading to an unequal level of information passing to the DNN training in different centrality bins.

C. Constituent quark number scaling

The study of the centrality and p_T dependence of v_2 for various identified particles seems incomplete without exploring its NCQ scaling behavior. By recalling our understanding of the specific mass ordering of $v_2(p_T)$ in the lower p_T regime, if the mass ordering is driven by a hydrodynamic pressure gradient, then $v_2(KE_T)$ at lower p_T should scale to a common set of values for all of the particles, which is indeed observed in experiments [59]. Here, $KE_T(= m_T - m_0)$ is the transverse kinetic energy, and $m_T(= \sqrt{p_T^2 + m_0^2})$ and m_0 are the transverse mass and rest mass of the particle, respectively. In the intermediate p_T regime, $v_2(KE_T)$ splits into two branches separately grouped by baryons and mesons. In this domain, the constituent quarks of the particles play a more substantial role in generating v_2 in hadrons than its mass. When the NCQ scaling is applied to $v_2(KE_T)$, it shows a better scaling behavior than $v_2(p_T)$ at lower p_T [16,59]. Figure 7 shows the centrality dependence of v_2/n_q as a function of KE_T/n_q. Here, the number of constituent quarks $n_q = 2$ for mesons and $n_q = 3$ for baryons. One can see that, at lower KE_T/n_q, the scaling is valid for all of the particle types. However, the proton seems to break the scaling at higher KE_T/n_q. The violation of KE_T scaling is observed in experiments, so the results from AMPT are in line [16,60]. Here, it is interesting to note that the DNN can learn particle-species-dependent scaling behavior as it closely agrees with the AMPT values for all energy and centrality classes.

D. Evolution of the crossing point

The separation of baryon-meson elliptic flow at the intermediate p_T is usually attributed to the quark

coalescence/recombination mechanism of hadronization. It suggests an apparent dependence of hadron flow on the number of constituent quarks of the hadron. This leads to a higher flow of baryons than mesons and a relative enhancement of baryon yield over meson yield in the intermediate-p_T regime. Now, by looking into the crossing point in p_T to know precisely where the separation of baryon-meson flow occurs, one can confirm the coalescence picture if the crossing occurs at somewhat higher transverse momenta for higher centralities. Figure 8 shows the centrality dependence of the p_T crossing point of the pion and proton elliptic flow for various collision systems at various energies. The vertical error bars represent the difference between the pion-proton and kaon-proton p_T crossing points. One can observe that the crossing point gradually shifts to higher p_T as one move from peripheral to central collisions for all collision energies. The shift of the curve to higher p_T with increasing energy could hint towards producing a denser partonic medium and the effect of increased radial flow with increasing collision energy. Here, the AMPT model qualitatively reproduces the trend of the p_T crossing curve as seen in the ALICE results. A similar observation is made from the DNN predictions, which also closely match the AMPT curves for the respective collision systems and energies. The DNN model not only learns the splitting of the elliptic flow into two branches grouped separately by baryons and mesons, but also preserves the same p_T crossing point of the separation, thus adding a more quantitative hold on the estimation of elliptic flow for identified charged hadrons.

E. Effect of transverse-momentum-dependent training on DNN

In Fig. 9, we present the predictions for elliptic flow as a function of transverse momentum from three different DNN models, each trained with a different set of inputs based on specific p_T cuts. These models are trained on the minimum bias Pb-Pb collisions at $\sqrt{s_{NN}} = 5.02$ TeV. For this investigation, the same model architecture with similar hyperparameter settings is used for training. The only difference would be the obtained weights and biases of the network for different p_T cuts.

The first row of Fig. 9 refers to the predictions from the DNN model trained with particle kinematic information for tracks in $|\eta| < 0.8$ with $p_T > 0.15$ GeV/c. We name it the unbiased case. It shows the evolution of $v_2(p_T)$ in (40–50)% central Pb-Pb collisions at $\sqrt{s_{NN}} = 5.02$ TeV, where the value of v_2 has a maximum around $2.0 \lesssim p_T|_{v_2^{max}} \lesssim 3.0$ GeV/c depending on the particle species. As the training is done for an unbiased range of p_T which also includes this $p_T|_{v_2^{max}}$, the DNN model seems to capture the overall trend of the $v_2(p_T)$ including the transition behavior around $p_T|_{v_2^{max}}$. Thus, the ratio of DNN to AMPT remains fairly close to unity for the entire p_T range (shown
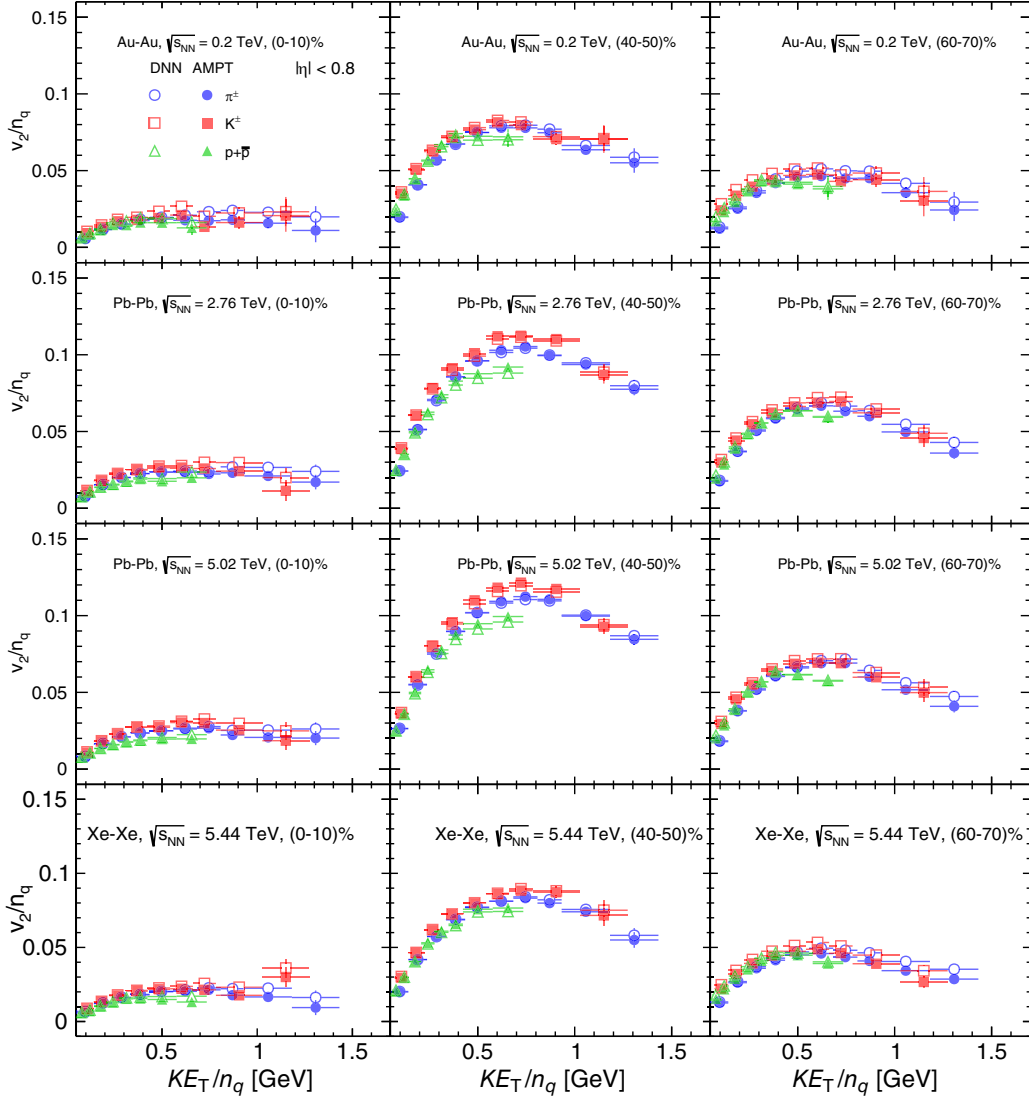
FIG. 7.   Centrality dependence of the constituent quark scaling of v_2 as a function of KE_T/n_q. The results from AMPT and the corresponding predictions from DNN are shown.
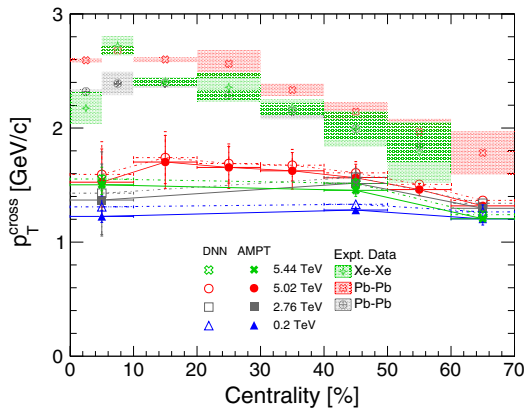

FIG. 8.   Centrality and energy-dependent evolution of the p_T crossing point, (p_T^{cross}) of baryon-meson elliptic flow in the intermediate-p_T regime. Here, the experimental data are obtained from the ALICE results [17,18,61].

up to 7 GeV/c) for all of the particle species. So far, all of the above-discussed results are obtained from the DNN model with this unbiased training.

Now we study the effect of training the DNN model in different transverse momentum regions. The aim is to obtain two different DNN models trained with and without the transition point of $p_T|_{v_2^{max}}$ and then test their applicability to the estimation of the $v_2(p_T)$ curve for the full range of p_T. We can obtain two groups of particles in an event based on the transverse momentum cuts applied to the tracks and we name them the low p_T cut group ($p_T^{Train} \leq 3.0$ GeV/c) and high p_T cut group ($p_T^{Train} > 3.0$ GeV/c). The estimation of elliptic flow is also performed using only these selected particles for the respective groups. The low p_T cut group includes the $p_T|_{v_2^{max}}$ and thus the transition behavior of $v_2(p_T)$ around $p_T|_{v_2^{max}}$. However, the high p_T cut group does not include this transition behavior directly from
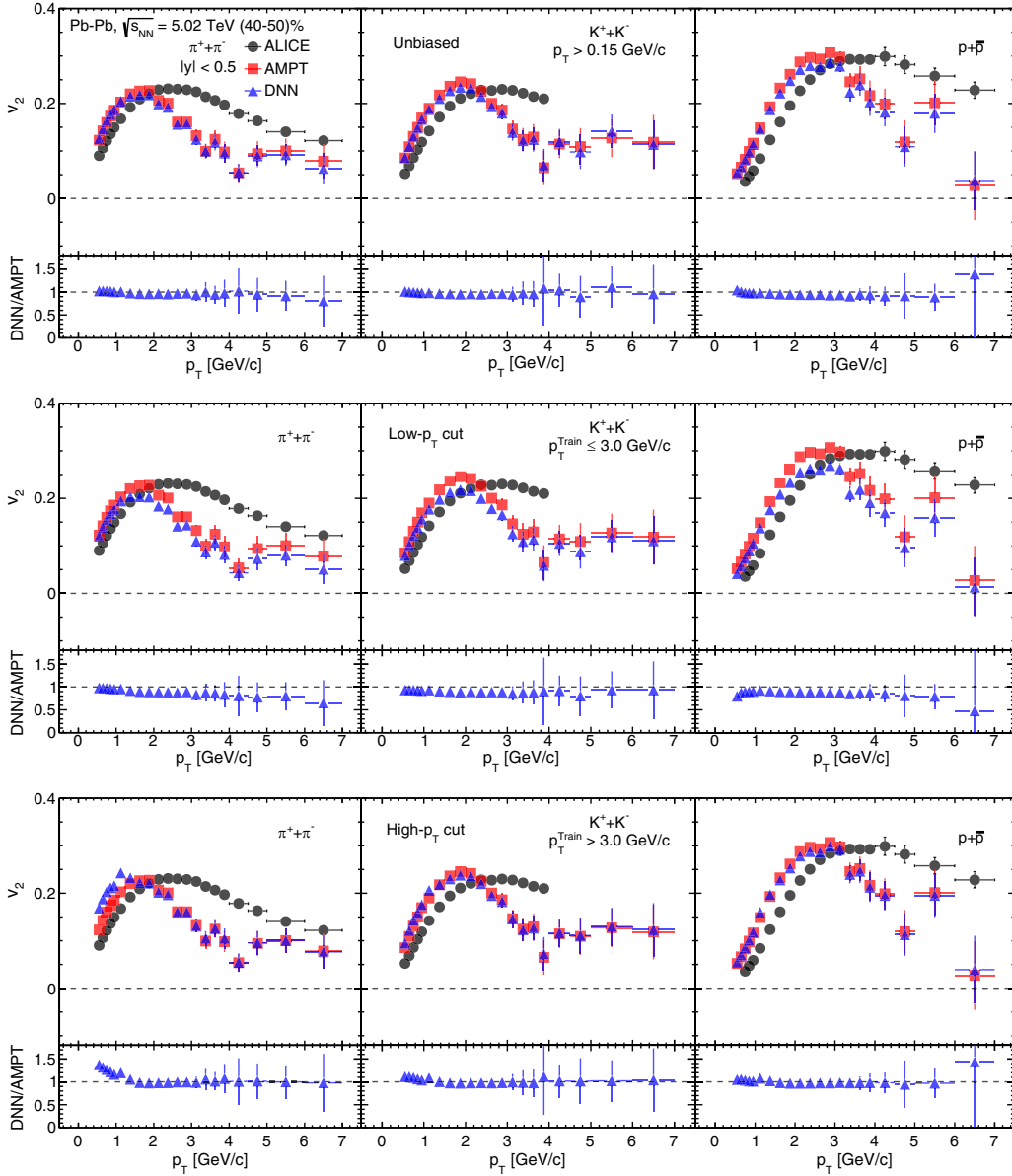
FIG. 9. Evaluation of DNN with transverse-momentum-dependent training applied to (40–50)% central Pb-Pb collisions at $\sqrt{s_{NN}} = 5.02$ TeV. Results for the models with unbiased ($p_T^{Train} > 0.15$ GeV/c), low-p_T cut group ($p_T^{Train} \leq 3.0$ GeV/c), and high-p_T cut group ($p_T^{Train} > 3.0$ GeV/c) particles are shown.

particle kinematics. After the training of these two separate DNN models with low-p_T and high-p_T particles from Pb-Pb collisions in $\sqrt{s_{NN}} = 5.02$ TeV minimum bias events, we apply each model to predict the entire $v_2(p_T)$ curve for the full range of p_T (shown up to 7 GeV/c) for the (40–50)% central Pb-Pb collisions at $\sqrt{s_{NN}} = 5.02$ TeV.

From the second and third rows of Fig. 9, it is quite interesting to see that both models, although being trained with two disjoint sets of particle groups, can successfully reproduce the entire $v_2(p_T)$ curve up to a reasonable extent in their respective cases. Somehow the models learn and complement the missing information of the $v_2(p_T)$ curve. For the low p_T cut group, the missing factor in training is

the high-p_T particles, and for the high p_T cut group, it is the low-p_T particles, and also the absence of the $p_T|_{v_2^{max}}$. As the information encoded in the network behaves like a generalized global curve of v_2 applicable to the entire p_T domain, the DNN models can extrapolate any regions of interest regardless of their training. This global curve learned by the DNN models represents the dependence of v_2 on transverse momentum and also its transition behavior around the $p_T|_{v_2^{max}}$. Although the mathematical function for such a curve is not available in the literature, the DNN can map this function from the existing input-output correlations irrespective of its training domain.

Another observation is the behavior of elliptic flow for different particle species. When the DNN model trained with low-p_T particles is applied to predict v_2 for the pion and kaon, a slight deviation is observed between DNN and AMPT starting from intermediate to high p_T. This is visible in the bottom ratio plots in the second row of Fig. 9. It hints that the elliptic flow for the pion and kaon primarily originates from low to intermediate p_T. However, in the same figure, the prediction for the proton deviates even at very low p_T, although the model includes this low-p_T region in training. It suggests that the contribution to elliptic flow for the proton mainly originates from high p_T. Thus, by removing this region in the low p_T cut DNN model, the accuracy is reduced for the entire curve for the proton v_2.

This hypothesis can be verified with the DNN model trained with high-p_T particles. One can see from the third row of Fig. 9 that the prediction of elliptic flow for proton is now more accurate for the entire p_T range as this DNN model includes high-p_T particles. This observation supports our earlier statement that the DNN captures a global curve of $v_2(p_T)$ and the proton v_2 has a dominant contribution from high p_T. However, in the same figure, pion and kaon elliptic flow deviates more for low p_T as the necessary contribution to elliptic flow is absent in this region for the high p_T cut model, and the same is visible in the ratio plots.

V. SUMMARY

To sum everything up that has been stated so far, this work demonstrates the applicability and accuracy of a DNN-based machine learning model to evaluate the second-order anisotropic flow coefficient (v_2) for identified particles from final-state particle kinematic information in heavy-ion collisions. The DNN model can eminently estimate v_2 for light-flavor identified particles such as $\pi^\pm$, $K^\pm$, and $p + \bar{p}$ in heavy-ion collisions at RHIC and LHC energies. The prediction accuracy of the DNN model is not only limited to Pb-Pb collisions at $\sqrt{s_{NN}} = 5.02$ TeV at which the model is trained, but is also applicable to other systems such as Pb-Pb collisions at $\sqrt{s_{NN}} = 2.76$ TeV, Xe-Xe collisions at $\sqrt{s_{NN}} = 5.44$ TeV, and Au-Au collisions at $\sqrt{s_{NN}} = 200$ GeV. From the minimum bias training, the model could successfully learn and preserve the

centrality, energy, and transverse momentum dependence of elliptic flow for other collision systems at various energies. This becomes a striking feature of DNN-based machine learning where, while dealing with multihadron production dynamics, the machine is trained with the control parameters like the collision energy, impact parameter (here, the number of participants or the final-state charged particle multiplicity), particle mass, and transverse momentum. In addition, the DNN model retains the constituent quark number scaling behavior for elliptic flow as a function of transverse kinetic energy for the respective collision systems and energies. The DNN model also quantitatively preserves the p_T crossing point of baryon-meson v_2 curves at intermediate p_T, which scales with the centrality and center-of-mass energy of collisions for various systems. Finally, by training the DNN models with different kinematic regions based on specific p_T cuts and then applying it to the full p_T range, we arrived at the conclusion that there exists a global functional dependence of elliptic flow on transverse momentum, as the DNN model trained in a certain kinematic region could describe the overall curve for the full kinematic domain. We also learned that the elliptic flow of the pion and kaon originates mainly from the low-p_T region, whereas the elliptic flow of the proton is dominated due to the high-p_T region.

[1] S. A. Bass, M. Gyulassy, H. Stoecker, and W. Greiner, J. Phys. G **25**, R1 (1999).

[2] U. Heinz and R. Snellings, Annu. Rev. Nucl. Part. Sci. **63**, 123 (2013).

[3] J. Adams *et al.* (STAR Collaboration), Phys. Rev. Lett. **92**, 052302 (2004).

[4] K. Aamodt *et al.* (ALICE Collaboration), Phys. Rev. Lett. **105**, 252302 (2010).

[5] K. Aamodt *et al.* (ALICE Collaboration), Phys. Rev. Lett. **107,** 032301 (2011).

[6] B. B. Abelev *et al.* (ALICE Collaboration), Phys. Rev. C **90,** 054901 (2014).

[7] P. F. Kolb, P. Huovinen, U. W. Heinz, and H. Heiselberg, Phys. Lett. B **500,** 232 (2001).

[8] S. A. Bass and A. Dumitru, Phys. Rev. C **61,** 064909 (2000).

[9] C. Nonaka and S. A. Bass, Phys. Rev. C **75,** 014902 (2007).

[10] D. Teaney, J. Lauret, and E. V. Shuryak, arXiv:nucl-th/0110037.

[11] T. Hirano, U. W. Heinz, D. Kharzeev, R. Lacey, and Y. Nara, Phys. Lett. B **636,** 299 (2006).

[12] S. A. Voloshin, Nucl. Phys. **A715,** 379 (2003).

[13] D. Molnar and S. A. Voloshin, Phys. Rev. Lett. **91,** 092301 (2003).

[14] H. Sato and K. Yazaki, Phys. Lett. B **98,** 153 (1981).

[15] C. B. Dover, U. W. Heinz, E. Schnedermann, and J. Zimanyi, Phys. Rev. C **44,** 1636 (1991).

[16] A. Adare *et al.* (PHENIX Collaboration), Phys. Rev. C **85,** 064914 (2012).

[17] B. B. Abelev *et al.* (ALICE Collaboration), J. High Energy Phys. 06 (2015) 190.

[18] S. Acharya *et al.* (ALICE Collaboration), J. High Energy Phys. 09 (2018) 006.

[19] A. M. Poskanzer and S. A. Voloshin, Phys. Rev. C **58,** 1671 (1998).

[20] N. Borghini, P. M. Dinh, and J. Y. Ollitrault, Phys. Rev. C **63,** 054906 (2001).

[21] R. S. Bhalerao, N. Borghini, and J. Y. Ollitrault, Nucl. Phys. **A727,** 373 (2003).

[22] R. S. Bhalerao, J. Y. Ollitrault, S. Pal, and D. Teaney, Phys. Rev. Lett. **114,** 152301 (2015).

[23] M. Hippert, D. Dobrigkeit Chinellato, M. Luzum, J. Noronha, T. Nunes da Silva, and J. Takahashi, Phys. Rev. C **101,** 034903 (2020).

[24] A. M. Sirunyan *et al.* (CMS Collaboration), Phys. Rev. C **96,** 064902 (2017).

[25] F. G. Gardim, F. Grassi, P. Ishida, M. Luzum, and J. Y. Ollitrault, Phys. Rev. C **100,** 054905 (2019).

[26] N. Mallick, S. Prasad, A. N. Mishra, R. Sahoo, and G. G. Barnaföldi, Phys. Rev. D **105,** 114022 (2022).

[27] Z. W. Lin, C. M. Ko, B. A. Li, B. Zhang, and S. Pal, Phys. Rev. C **72,** 064901 (2005).

[28] X. N. Wang and M. Gyulassy, Phys. Rev. D **44,** 3501 (1991).

[29] B. Zhang, Comput. Phys. Commun. **109,** 193 (1998).

[30] Z. w. Lin and C. M. Ko, Phys. Rev. C **65,** 034904 (2002).

[31] Y. He and Z. W. Lin, Phys. Rev. C **96,** 014910 (2017).

[32] B. Li, A. T. Sustich, B. Zhang, and C. M. Ko, Int. J. Mod. Phys. E **10,** 267 (2001).

[33] B. A. Li and C. M. Ko, Phys. Rev. C **52,** 2037 (1995).

[34] R. J. Fries, B. Muller, C. Nonaka, and S. A. Bass, Phys. Rev. Lett. **90,** 202303 (2003).

[35] R. J. Fries, B. Muller, C. Nonaka, and S. A. Bass, Phys. Rev. C **68,** 044902 (2003).

[36] V. Greco, C. M. Ko, and P. Levai, Phys. Rev. C **68,** 034904 (2003).

[37] S. Tripathy, S. De, M. Younus, and R. Sahoo, Phys. Rev. C **98,** 064904 (2018).

[38] N. Mallick, R. Sahoo, S. Tripathy, and A. Ortiz, J. Phys. G **48,** 045104 (2021).

[39] N. Mallick, S. Tripathy, A. N. Mishra, S. Deb, and R. Sahoo, Phys. Rev. D **103,** 094031 (2021).

[40] S. Prasad, N. Mallick, S. Tripathy, and R. Sahoo, arXiv:2207.12133.

[41] C. Loizides, J. Kamin, and D. d'Enterria, Phys. Rev. C **97,** 054910 (2018); **99,** 019901(E) (2019).

[42] S. Voloshin and Y. Zhang, Z. Phys. C **70,** 665 (1996).

[43] M. Masera, G. Ortona, M. G. Poghosyan, and F. Prino, Phys. Rev. C **79,** 064909 (2009).

[44] P. C. Bhat, Annu. Rev. Nucl. Part. Sci. **61,** 281 (2011).

[45] B. P. Roe, H. J. Yang, J. Zhu, Y. Liu, I. Stancu, and G. McGregor, Nucl. Instrum. Methods Phys. Res., Sect. A **543,** 577 (2005).

[46] P. Baldi, P. Sadowski, and D. Whiteson, Nat. Commun. **5,** 4308 (2014).

[47] P. Baldi, P. Sadowski, and D. Whiteson, Phys. Rev. Lett. **114,** 111801 (2015).

[48] A. Buckley, A. Shilton, and M. J. White, Comput. Phys. Commun. **183,** 960 (2012).

[49] M. Bridges, K. Cranmer, F. Feroz, M. Hobson, R. Ruiz de Austri, and R. Trotta, J. High Energy Phys. 03 (2011) 012.

[50] G. Bíró, M. Pocsai, I. F. Barna, G. G. Barnaföldi, J, T. Moody, and G. Demeter, Opt. Laser Technol. **159,** 108948 (2023).

[51] X. Glorot, A. Bordes, and Y. Bengio, *Proceedings of the Fourteenth International Conference on Artificial Intelligence and Statistics, Ft. Lauderdale, USA, PMLR Workshop and Conference Proceedings* (2011), pp. 315–323, https://proceedings.mlr.press/v15/glorot11a.html.

[52] D. P. Kingma and J. Ba, arXiv:1412.6980.

[53] Available online: https://www.intel.com/content/www/us/en/products/sku/191070/intel-core-i58279u-processor-6m-cache-up-to-4-10-ghz/specifications.html.

[54] F. Chollet *et al.*, https://keras.io/.

[55] M. Abadi, A. Agarwal, P. Barham, E. Brevdo, Z. Chen, C. Citro, G. S. Corrado, A. Davis, J. Dean, M. Devin *et al.*, arXiv:1603.04467.

[56] F. Pedregosa *et al.*, J. Mach. Learn. Res. **12,** 2825 (2011).

[57] J. Tian, J. H. Chen, Y. G. Ma, X. Z. Cai, F. Jin, G. L. Ma, S. Zhang, and C. Zhong, Phys. Rev. C **79,** 067901 (2009).

[58] G. Song and W. Chai, arXiv:1805.11761.

[59] A. Adare *et al.* (PHENIX Collaboration), Phys. Rev. Lett. **98,** 162301 (2007).

[60] N. Mallick, S. Tripathy, and R. Sahoo, Eur. Phys. J. C **82,** 524 (2022).

[61] S. Acharya *et al.* (ALICE Collaboration), J. High Energy Phys. 10 (2021) 152.